Plasma Phys. Control. Fusion **60** (2018) 014029 (12pp) https://doi.org/10.1088/1361-6587/aa8c50

On the feasibility of sub-100 nm rad emittance measurement in plasma accelerators using permanent magnetic quadrupoles

F Li[1], Y P Wu[1], Z Nie[1], B Guo[1], X H Zhang[1,2], S Huang[1,2], J Zhang[1,2], Z Cheng[1], Y Ma[1,2], Y Fang[1], C J Zhang[3], Y Wan[1], X L Xu[3], J F Hua[1], C H Pai[1], W Lu[1] and Y Q Gu[2]

[1] Department of Engineering Physics, Tsinghua University, Beijing 100084, People's Republic of China
[2] Laser Fusion Research Center, China Academy of Engineering Physics, Mianyang, Sichuan 621900, People's Republic of China
[3] University of California Los Angeles, Los Angeles, CA 90095, United States of America

E-mail: jfhua@tsinghua.edu.cn and weilu@tsinghua.edu.cn

Received 30 June 2017, revised 23 August 2017
Accepted for publication 13 September 2017
Published 2 November 2017

Abstract

Low emittance (sub-100 nm rad) measurement of electron beams in plasma accelerators has been a challenging issue for a while. Among various measurement schemes, measurements based on single-shot quad-scan using permanent magnetic quadrupoles (PMQs) has been recently reported with emittance as low as ∼200 nm Weingartner (2012 *Phys. Rev. Spec. Top. Accel. Beams* **15** 111302). However, the accuracy and reliability of this method have not been systematically analyzed. Such analysis is critical for evaluating the potential of sub-100 nm rad emittance measurement using any scheme. In this paper, we analyze the effects of various nonideal physical factors on the accuracy and reliability using the PMQ method. These factors include aberration induced by a high order field, PMQ misalignment and angular fluctuation of incoming beams. Our conclusions are as follows: (i) the aberrations caused by high order fields of PMQs are relatively weak for low emittance measurement as long as the PMQs are properly constructed. A series of PMQs were manufactured and measured at Tsinghua University, and using numerical simulations their high order field effects were found to be negligible . (ii) The largest measurement error of emittance is caused by the angular misalignment between PMQs. For low emittance measurement of ∼100 MeV beams, an angular alignment accuracy of 0.1° is necessary. This requirement can be eased for beams with higher energies. (iii) The transverse position misalignment of PMQs and angular fluctuation of incoming beams only cause a translational and rotational shift of measured signals, respectively, therefore, there is no effect on the measured value of emittance. (iv) The spatial resolution and efficiency of the detection system need to be properly designed to guarantee the accuracy of sub-100 nm rad emittance measurement.

Keywords: emittance measurement, permanent magnetic quadrupole, plasma-based acceleration

(Some figures may appear in colour only in the online journal)

1. Introduction

Plasma-based acceleration (PBA) [2, 3] has received extensive attention in recent years because it has the capability of delivering high energy electron beams [4–7] and has ideal field properties [8, 9] to accelerate high quality beams in a very compact setup. This makes PBA a promising candidate for compact light sources and future colliders. The generation of high quality electron beams in PBA is one of the critical issues for these applications. Emittance is an important figure of merit for evaluating beam quality. Although electron beams with low emittance have been observed experimentally [1, 10–13] and the generation of sub-100 nm rad emittances in PBA has also been predicted through simulations [14–17], there is still a lack of effective approaches to measure such low emittances. Especially for the PBA beams, there are issues of beam matching from plasma to conventional beamlines and the transport of beams with extremely small source size ($\lesssim 1\ \mu$m). This leads to emittance measurement becoming more challenging compared with conventional accelerators [18, 19]. Previous emittance measurements of PBA electron beams mainly utilized pepper-pots [11, 20, 21], betatron radiation [10, 12, 13, 22], inverse-Compton-scattered x-rays [23] and miniature permanent quadrupole magnets [1, 24]. Measurements of μm-class normalized emittance have been reported using a miniature pepper-pot. However, this method can provide very inaccurate results when the size of the source is below $\sim$10 μm [25]. Moreover, it relies on a low energy spread to yield meaningful normalized emittances and the structure thickness sets an upper limit for the measurable beam energy. Characterizing the betatron radiation emitted by the electron beams in plasma enables us to determine the beam size. Combining the divergence measurement, the beam emittance can be estimated. However, this indirect method assumes a matched beam and neglects the emittance growth within the plasma–vacuum transition. Therefore, the evolution of emittance during beam transport cannot be accomplished using this method. Miniature permanent magnetic quadrupoles (PMQs) with very high field gradients have been applied in PBA in recent years. A single-shot quadrupole scan has been proposed and demonstrated experimentally using PMQs in combination with a dipole magnet, which performs direct measurement of PBA beams [1]. This method can simultaneously measure geometry emittance ϵ_x, Twiss parameters and resolve the energy spectrum (and thus obtain the average relativistic factor $\langle\gamma\rangle$ and the relative energy spread σ_γ). Therefore the normalized emittance $\epsilon_{n,x}$ can be directly derived according to $\epsilon_n^2 \simeq \langle\gamma\rangle^2(\sigma_\gamma^2\sigma_{x0}^2\sigma_{x0}'^2 + \epsilon_x^2)$ [18], where σ_{x0} and σ'_{x0} are the initial beam size and divergence. This is one of the major advantages over other methods that are not spectrally resolved. Although experiments have demonstrated $\sim$0.2 μm normalized emittance measured with this method, the reliability of the method and the feasibility of low emittance measurement have not been systematically reported in the current literature. This paper aims to answer the question and clarify some of the limits of the method before applying it to sub-100 nm rad emittance measurements in PBA.

This paper is organized as follows: section 2 briefly introduces the basic principle of the single-shot version of quadrupole scan measurement. Section 3 mainly discusses the impacts of several nonideal factors in experiments on the measurement of beam emittance. Conclusions are drawn in the last section.

2. Single-shot emittance measurement with quadrupole magnets

The transverse phase space of electron beams is often characterized by Twiss parameters α_x, β_x, γ_x and the natural emittance is defined by $\epsilon_x \equiv \sqrt{\langle x^2\rangle\langle x'^2\rangle - \langle xx'\rangle^2}$, where x and x' represent the transverse position and direction, respectively. These parameters describe the area and orientation of the electron distribution in the phase space. In a beam transport system, the transverse position and direction of a single particle (x, x') at s is connected to the initial values (x_0, x_0') at s_0 by the transport matrix $\mathbf{M}_x$, i.e. $(x, x')^T = \mathbf{M}_x(x_0, x_0')^T$. The variation in Twiss parameters can be also expressed in a matrix format [26]:

$$\begin{pmatrix}\beta_x\\ \alpha_x\\ \gamma_x\end{pmatrix} = \begin{pmatrix} M_{x,11}^2 & -2M_{x,11}M_{x,12} & M_{x,12}^2\\ -M_{x,11}M_{x,21} & M_{x,11}M_{x,22} + M_{x,21}M_{x,12} & -M_{x,12}M_{x,22}\\ M_{x,21}^2 & -2M_{x,21}M_{x,22} & M_{x,22}^2 \end{pmatrix} \times \begin{pmatrix}\beta_{x0}\\ \alpha_{x0}\\ \gamma_{x0}\end{pmatrix}, \tag{1}$$

where $M_{x,ij}$ refers to the element of the transport matrix M_x. Therefore the beam size $\sigma_x(s)$ is connected to the initial Twiss parameters, transport matrix and beam emittance as

$$\sigma_x(z)^2 = \beta_x\epsilon_x = \epsilon_x(M_{x,11}^2\beta_{x0} - 2M_{x,11}M_{x,12}\alpha_{x0} + M_{x,12}^2\gamma_{x0}). \tag{2}$$

For the conventional quadrupole scan method, one needs to change the excitation currents (if using electromagnets) or the magnets' positions to achieve the multi-shot measurement. However, since the electron beams produced by the plasma-based acceleration are not as stable as the state-of-art RF accelerators, multi-shot measurements are difficult to apply and a single-shot method is necessary. Considering that the transport matrix is a function of the particle energy γ and the generated beams have natural energy spreads, the single-shot method can be realized by measuring $\sigma_x(s)$ for different particle energies. In order to achieve this, an energy-dispersed component (dipole magnet) must be introduced to enable the system to have the spectrum resolution. After determining the $\sigma_x - \gamma$ relationship, equation (2) can be solved in the using the least square method (see appendix A). Figure 1(a) shows a sketch of the experimental setup. The reference particles are well focused by the quadrupole magnets and thus appear as very small σ_x on the detection screen. The fractions with energies deviating from the reference particles have larger σ_x. Therefore the signals observed on the screen appear like a 'bowtie' with the reference particles forming the 'knot' as shown in figure 1(b).

To increase the pointing stabilization of the signals on the screen, the transport system is usually designed such that $M_{12} = 0$ in both the x and y directions for the reference particles. According to equation (2), the beam size of the reference particles is irrelevant to its initial divergence $\sigma'_{x0} = \sqrt{\gamma_{x0}\epsilon_x}$ and the initial phase space orientation is determined by α_{x0}. In this

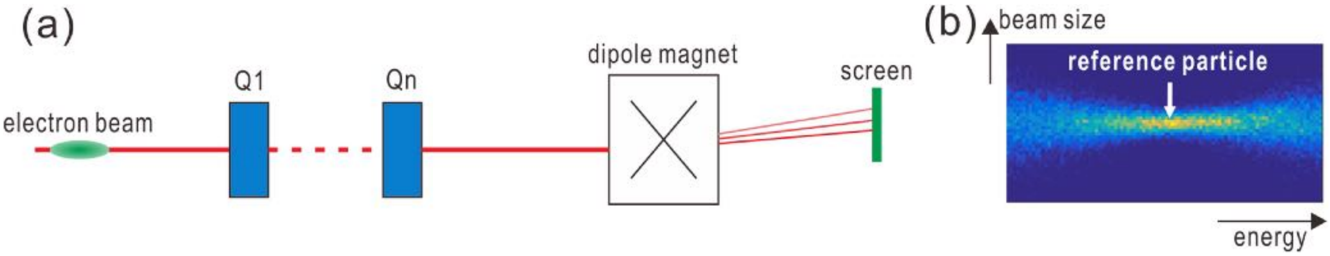

Figure 1. (a) Sketch of the single-shot emittance measurement using PMQs. The electron beam passing through the focusing system composed of n PMQs is bent by the dipole magnet and finally collected by the detection screen. (b) Typical bowtie-shaped signal shown on the screen.

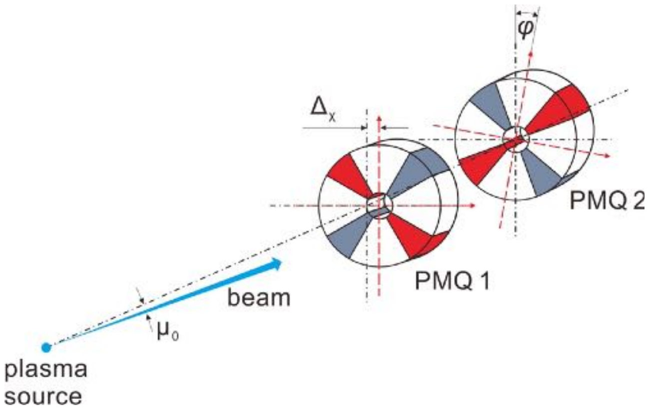

Figure 2. Error sources of emittance measurement using PMQs. In this plot, the transverse position of the first PMQ is misaligned with an offset of Δ_x. The second PMQ has an azimuthal angular orientation of φ. The emission angle of the outgoing beam is μ_0 due to shot-to-shot pointing fluctuation.

case, $\sigma_{x,\mathrm{ref}}^2 = \epsilon_x M_{x,11}^2 \beta_{x0} = M_{x,11}^2 \sigma_{x0}^2$ where $|M_{x,11}|$ acts as the magnification. For the electron beams generated in the plasma-based acceleration, since σ_{x0} is frequently on the (sub-) micrometer level, magnifications of tens of times are therefore needed.

It is worth noting that this method assumes implicitly that the initial beam emittance does not correlate to the energy. For the majority of the PBA beams, this assumption is approximately satisfied. Even for those with a correlation between the beam energy and geometry emittance, this method still provides a good estimation of the upper limit. The rationality of this assumption will be discussed in section 3.6.

3. Factors influencing emittance measurements

PMQs with a small aperture can reach very high magnetic field gradients [27, 28] which are applicable for the transport of PBA electron beams. However, small apertures pose challenges in the manufacture, setup and characterization of the magnets. Manufacturing imperfections and misalignments during the setting up of the beamline introduce errors into the final results of the beam emittance. On the other hand, due to the angular fluctuation of the output electron beams, the incident transverse positions varies shot to shot, which may also impact the measured results. Figure 2 illustrates the error sources including position misalignment, azimuthal angular orientation and pointing fluctuation. We point out that the influences brought by these nonideal factors could be more significant when compared with the traditional accelerator scenario because of the more compact magnet structures and relatively unstable beams. In this case, the tolerances to these nonideal factors ought to be carefully discussed especially for the case of very low emittances. In addition, resolution and detection efficiency is another important experimental consideration and will be discussed in this section.

3.1. High order field components (HOFCs)

Multipole field components higher than the quadrupole field component exert nonlinear forces on electron beams, thus eventually distorting the phase space and increasing the emittance. These HOFCs will inevitably be introduced during machining and assembly. Whether the HOFCs will significantly impact the measurement of beam emittance in PBA should be determined.

Using the polar coordinates, the assumption of $B_z = 0$ leads to the magnetic field and can be expanded as

$$\mathbf{B}(\rho,\,\phi) = \sum_{k=1}^{\infty} [B_{k\rho}(\rho,\,\phi)\hat{\mathbf{e}}_\rho + B_{k\phi}(\rho,\,\phi)\hat{\mathbf{e}}_\phi], \tag{3}$$

with

$$B_{k\rho} = \rho^{k-1}[A_k \sin(k\phi) + B_k \cos(k\phi)] \tag{4}$$

$$B_{k\phi} = \rho^{k-1}[A_k \cos(l\phi) - B_k \sin(k\phi)], \tag{5}$$

where k is the harmonic number of the multipole fields and A_k and B_k are the Fourier coefficients. The magnitude and phase of each harmonic are defined as $\sqrt{A_k^2 + B_k^2}$ and $\tan^{-1}(B_k/A_k)$.

To examine the practical impact brought by the HOFCs, we fabricated a series of miniature Halbach-type [29] PMQs. As shown in figure 3, there are 12 small trapezoidal magnetic wedges made of neodymium iron boride (NdFeB) assembled in a single PMQ. When coupling these wedges together, an aluminum alignment tube with a bore size of 6 mm was used. The wedge array is enclosed by 12 pieces of yoke irons which both confine the magnetic fields and bear the pressure from the locking screws outside.

For simplicity, we used a pair of PMQs. The focusing (in x direction) magnet (Q1) with an effective length of 19.6 mm

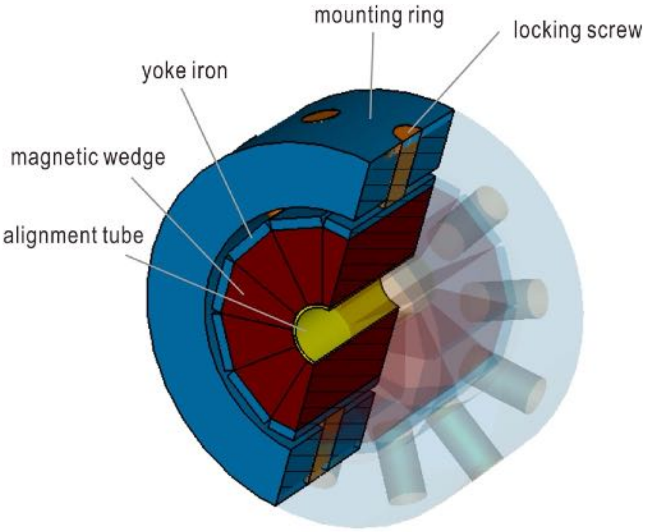

Figure 3. CAD drawing of the PMQs.

has a measured field gradient of $\sim$284 T/m. The defocusing magnet (Q2) has a longer effective length of 14.9 mm and its field gradient is $\sim$199 T/m. The characterization of the magnets, including field gradients, linearity and HOFCs, is conducted using the Hall probe method described in reference [30] as well as the oscillating wire method [31]. The measured results are shown in figure 4. We carried out numerical simulations to examine the impacts of the HOFCs. In the simulations, for a given magnification of $|M_{x,11}| = 20$, electron beams of 2.7 μm rad and 54 nm rad normalized emittances with different energies and a fixed rms energy spread of 5% were examined. The beamline parameters are listed in table 1.

The measured PMQ parameters are imported directly into the simulations. The signals on the screen are simulated for the cases of the switching on and off the HOFCs. The witness beams have a fixed initial beam size ($\sigma_{x0} = 5\ \mu$m for beams of $\epsilon_{n,x} = 2.7\ \mu$m rad and $\sigma_{x0} = 0.5\ \mu$m for those of $\epsilon_{n,x} = 54$ nm rad). The remainder of the paper uses the same parameters, and thus the initial divergence decreases when increasing the beam energy. As shown in figures 5(a) and (b), the beam sizes on the detection screen with HOFCs present little difference from those using ideal PMQs for both 2.7 μm rad and 54 nm rad emittances. Figure 5(c) shows the relative errors of the emittance measurement. When increasing the beam energy, there is a downward trend in the relative error. This is because the magnitudes of the HOFCs are proportional to ρ^{k-1} which implies that the particles at a larger ρ feel larger nonlinear forces. For this reason, the aberration caused by the HOFCs has less impact on the beams of smaller incident transverse size. For the same reason, the relative error for the beams of 54 nm rad emittance is lower than those of 2.7 μm rad emittance. The results shown in figure 5 indicate the HOFCs of the manufactured magnets have an insignificant impact on the emittance measurements.

We also carry out simulations to examine the impact of a separate HOFC and then give a rough estimation of the tolerance of each HOFC. Figure 6 shows the measurement errors for different relative strengths of the sextupole and octupole components. The relative strength is defined as the ratio between the magnitude of a certain HOFC and that of the quadrupole component, i.e. $\sqrt{A_k^2 + B_k^2}\Big/\sqrt{A_2^2 + B_2^2}$. In the simulations, the phases of the HOFCs $\tan^{-1}(B_k/A_k)$ are assumed to be zero. As one can see, in order to achieve errors less than 10% for the measurement of $\sim$100 MeV beams, the relative strengths of the sextupole and octupole components should be controlled within $\sim$0.005 mm^{-1} and $\sim$0.002 mm^{-2} for the beams of $\epsilon_{n,x} = 2.7\ \mu$m rad, and within $\sim$0.02 mm^{-1} and $\sim$0.03 mm^{-2} for those of $\epsilon_{n,x} = 54$ nm. This requirement is within the reach of current technical conditions. For higher beam energies and lower emittances, this restriction can be further eased.

The examples above indicate that the small-aperture PMQs under current technical conditions have the capability of measuring sub-100 nm rad emittance. Finetuning the magnetic wedges [30] or using more wedges can improve the quality of the magnetic field so that the errors induced by the HOFCs can be further reduced.

3.2. Angular misalignment of PMQs

Misalignments are unavoidable during the setting up the beamline. One of the major sources of errors is the angular misalignment of PMQs. We still use the same beamline setup and initial beam parameters mentioned above to examine this error source. In the simulations, the first PMQ was rotated by a small angle φ_1 and the other components were kept ideal, where φ_i is the rotational angle of the ith PMQ. It can be seen from the results shown in figures 7(a) and (b) that for beam emittances of both 2.7 μm rad and 54 nm rad, the appearance of the angular misalignment that leads to σ_x becomes bigger. Figure 7(c) shows the emittance errors versus φ_1 for different beam energies and emittances. The measurement errors of $\epsilon_{n,x} = 54$ nm rad are significantly bigger than those of $\epsilon_{x,n} = 2.7\ \mu$m rad even though the beamline and PMQs are identical. The measurement errors are less sensitive to higher beam energies, and agree with our estimations. To get acceptable errors, say below 20%, $\varphi_i < 0.2°$ for the 2.7 μm rad beams and $\varphi_i < 0.1°$ for the 54 nm rad beams are required. Measuring electron beams of higher energies can further ease the limit.

The measurement errors essentially originate from the coupled motions between the x and y directions which are brought by the rotation of quadrupole magnets. In this case, we need to discuss the beam motion in the 4D phase space (x, x', y, y'). Appendix B provides a detailed analysis of the system error induced by the angular misalignments and the error can be estimated by

$$\sigma_{\epsilon_x}^2 = \frac{1}{4}\frac{\sum_i ((\mathbf{S}_x^{-1}\Delta\mathbf{S}_{xy}^{(i)}\tilde{\mathbf{T}}_y)^T\mathbf{\Lambda}\tilde{\mathbf{T}}_x + \tilde{\mathbf{T}}_x^T\mathbf{\Lambda}\mathbf{S}_x^{-1}\Delta\mathbf{S}_{xy}^{(i)}\tilde{\mathbf{T}}_y)^2\sigma_{\varphi_i^2}^2}{\tilde{\mathbf{T}}_x^T\mathbf{\Lambda}\tilde{\mathbf{T}}_x}, \tag{6}$$

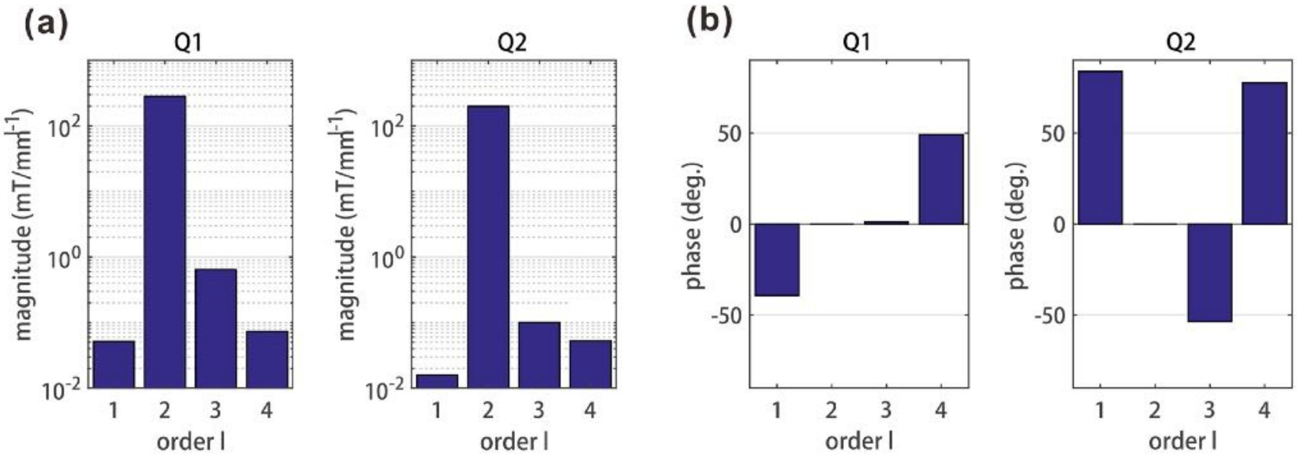

Figure 4. Measured magnitudes (a) and phases (b) of magnetic field components. Here $k = 1, 2, 3, 4$ refer to the dipole, quadrupole, sextupole and octupole field components, respectively.

Table 1. Beamline parameters for different beam energies. L_1, L_2 and L_3 are the distances from the plasma source to Q1, from Q1 to Q2 and from Q2 to the detection screen.

Beam energy (MeV)	L_1 (mm)	L_2 (mm)	L_3 (mm)
55	44.7	36.8	538.1
100	83.7	78.3	943.6
150	127.1	124.7	1393.4
200	170.5	171.1	1843.0
250	213.8	217.5	2292.5
300	257.2	264.0	2741.9
350	300.6	310.5	3191.4

where $\sigma_{\varphi_i^2}$ is the error of φ_i^2 for the ith PMQ, φ_i is the rotation angle, 3×3 matrices $\mathbf{S}_x$ and $\Delta_{xy}^{(i)}$ are solely determined by the ideal transport matrix of each component. The Twiss parameters vectors $\tilde{\mathbf{T}}_u = \epsilon_u(\beta_{u0}, \gamma_{u0}, \alpha_{u0})^T$ $(u = x, y)$ are obtained experimentally. Once the parameters of all the components in the beamline and the angular errors for each PMQ areknown, one can estimate the emittance error. The dotted lines in figure 7 are calculated with equation (6) and agree well with the simulation results.

3.3. Position misalignment of PMQs

Another kind of experimental setup error is the position misalignments of PMQs in the transverse directions. This error can be caused during the beamline setup, but also by the magnetic center not overlapping with the geometric center of the PMQs. However, it can be proven (see appendix C) that the measured beam size is irrelevant to the position misalignments and thus the accuracy of the emittance measurement will not be affected. In fact, such setup misalignment will cause the beam spots to shift on the screen. Too large of offsets of the PMQs caused the beam loss because of hitting on the beam holes.

In order to verify the inference in appendix C, we carried out simulations and set the offset of the first PMQ in the x direction to be 50 and 100 μm. Figure 8 shows the results. The signals on the screen are shifted and the offsets are the same for a given Δ_x regardless of the initial beam emittance. Figures 8(d) and (h) show that the beam sizes with respect to γ are exactly the same for different Δ_x. This indicates that the measured emittances are independent of Δ_x, which agrees with the theory.

3.4. Angular fluctuation of incoming beams

A typical angular fluctuation of a PBA electron beam is $\sim$mrad level. How oblique incidence affects the emittance measurement should be clarified as well. Considering an electron beam with a nonzero initial emission angle $\mu_0 = \langle x_0' \rangle$, the average beam position of the detection screen is therefore $\langle x \rangle = M_{x,12}\mu_0$ according to the relationship $x = M_{11,x}x_0 + M_{12,x}x_0'$. Centralizing x and x_0', i.e. $\tilde{x} = x - M_{x,12}\mu_0$ and $\tilde{x}_0' = x_0' - \mu_0$, yields $\tilde{x} = M_{11,x}x_0 + M_{x,12}\tilde{x}_0'$ and the beam size on the screen

$$\begin{aligned}\sigma_{\tilde{x}}^2 &= M_{x,11}^2\langle x_0^2 \rangle + M_{x,12}^2\langle \tilde{x}_0^2 \rangle + 2M_{x,11}M_{x,12}\langle x_0\tilde{x}_0' \rangle \\ &= \epsilon_x(M_{x,11}^2\beta_{x0} + M_{x,12}^2\gamma_{x0} - 2M_{x,11}M_{x,12}\alpha_{x0}). \qquad (7)\end{aligned}$$

The beam size is the same as the case of a normal incident beam, so the emittance measurement is not affected by the angular fluctuation of beams.

To verify the deduction above, numerical simulations are conducted for normal and obliquely incident electron beams into an ideal beamline. As shown in figure 9, the measured beam size $\sigma_{\tilde{x}}$ is the same for different μ_0 as well as the retrieved emittances. Interestingly, the skew angle of the detected signals varies for different μ_0 because of the signal offset $\Delta_x = M_{x,12}\mu_0$. For the reference particles $M_{x,12} = 0$ so the center of the signals does not change, while for the fractions with energy $\gamma = \gamma_0 + \Delta\gamma$ the center of the signal shifts due to the dependence of $M_{x,12}$ on γ. It is easy to show that the skew angle of the detected signal is $\theta_r = \tan^{-1}(\partial_\gamma M_{x,12}(\gamma_0)\mu_0/R_\gamma)$ where R_γ is the spectral resolution. Therefore the angular fluctuation can be deduced through the statistics of θ_r.

It is worth noting that the PMQs having a tilt angle also causes the oblique incidence of beams, but the tilt angle can be controlled on the μrad level, which can be fully neglected.

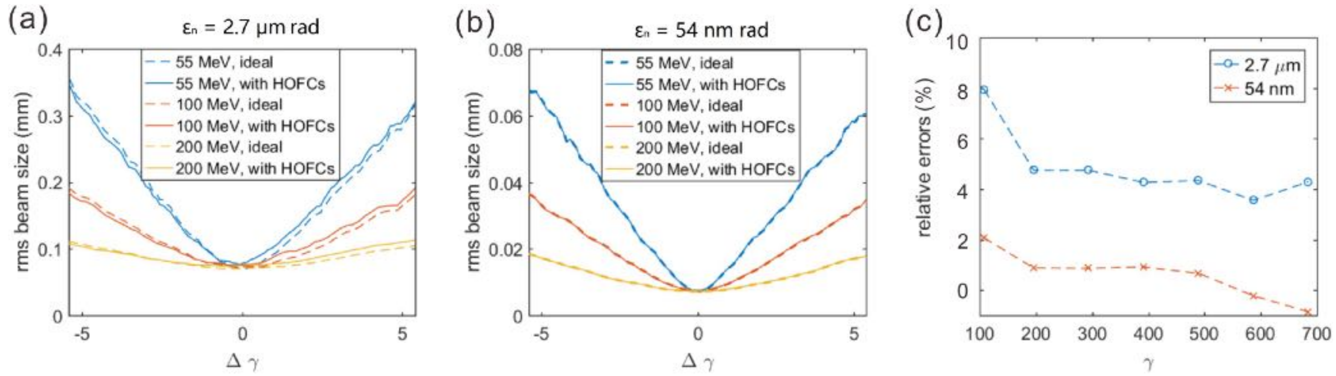

Figure 5. Signals on the detection screen for the ideal PMQs and HOFCs presented. Beam sizes σ_x as a function of particle energy are plotted in (a) and (b) for beams of 2.7 μm rad and 54 nm rad normalized emittances, respectively. $\Delta\gamma = \gamma - \gamma_0$ is the energy offset with respect to the average energy γ_0. Plot (c) shows the relative errors of the retrieval emittances for different γ. To generate these plots, 1×10^5 particles satisfying the bi-Gaussian distribution in the transverse phase space are simulated. Information on these test particles is obtained by solving the Newton equation.

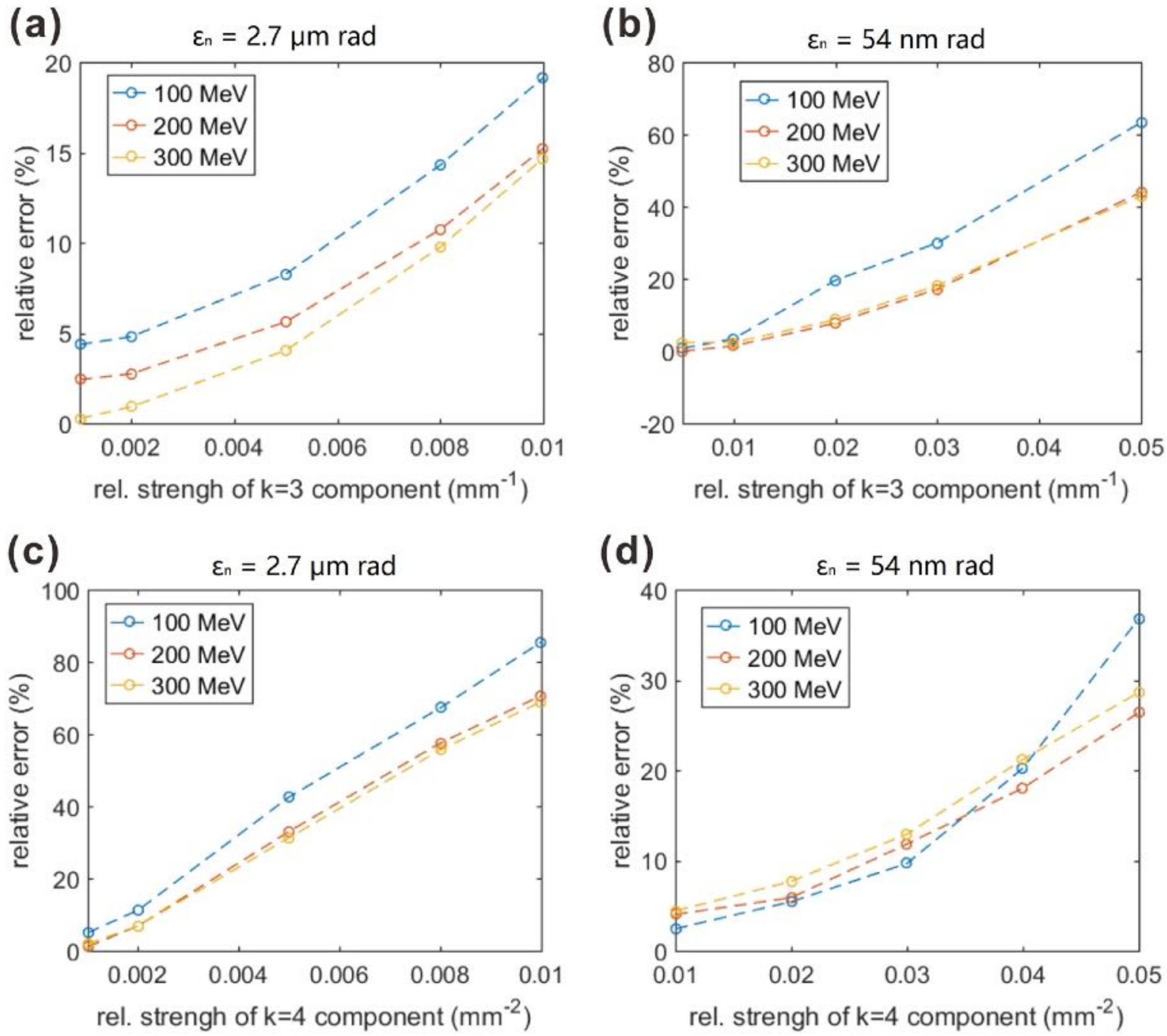

Figure 6. Emittance errors versus the magnitudes of the sextupole (a)–(b) and octupole (c)–(d) components for beams of different energies and emittances. The normalized emittance is 2.7 μm rad in plots (a) and (c) and 54 nm rad in plots (b) and (d).

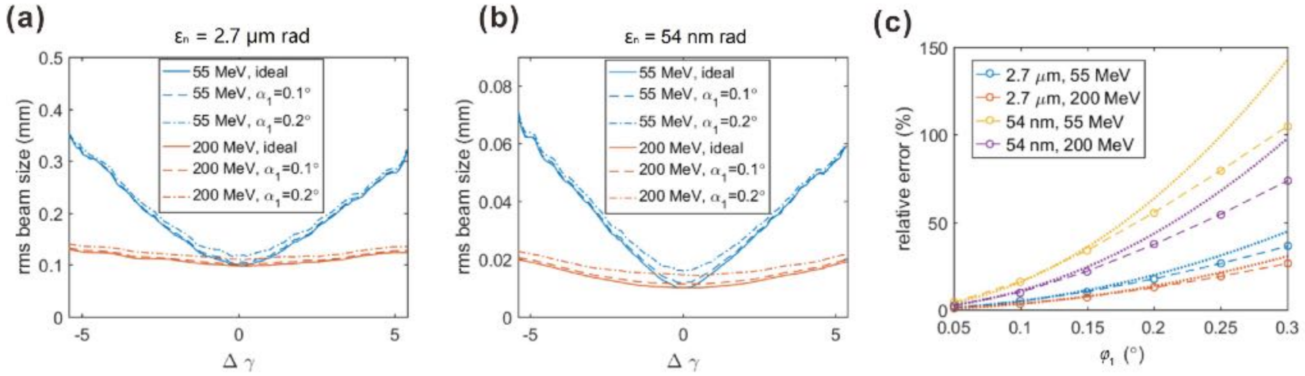

Figure 7. The relations between the beam size σ_x and the energy offset $\Delta\gamma = \gamma - \gamma_0$ for $\epsilon_{n,x} = 2.7$ μm rad (a) and $\epsilon_{n,x} = 54$ nm rad (b). Plot (c) shows the relative emittance errors versus φ_1. The dotted lines are the corresponding theoretical estimations. The beams of $\epsilon_{n,x} = 2.7$ μm rad have a fixed initial size $\sigma_{x0} = 5$ μm and those of $\epsilon_{n,x} = 2.7$ μm rad have fixed $\sigma_{x0} = 0.5$ μm for different energies. The beamline setups are the same with those in table 1.

3.5. Spatial resolution and detection efficiency

For the sub-100 nm rad emittance measurements, the beam size on the detection screen is frequently several microns because of the extremely small initial beam size on the sub-μm level, even if several ten times of magnification is applied. Therefore the spatial resolution required would be on the micron level. However, there are a number of factors that will degrade the spatial resolution, including the multiple Coulomb scattering, the transparency of the scintillating material and the resolution of an optical imaging system. A particle will experience multiple scattering when traveling through the detection screen. The divergence caused by the multipole Coulomb scattering can by estimated by [32] $\theta_C = \frac{13.6\ \mathrm{MeV}}{\beta cp}\sqrt{d/\lambda_0}\,(1 + 0.038\ln(d/\lambda_0))$, where β is the normalized velocity, p is the momentum, d is the thickness of the scintillating material and λ_0 is the radiation wavelength. The rms width of the point spread function (PSF) for this effect is therefore $\sigma_s \simeq \theta_C d$. If the screen is transparent, the scintillating material radiates along the whole particle path and at all angles. This will also deteriorate the spatial resolution and the width of the PSF is [33] $\sigma_f \simeq \frac{d}{n}\mathrm{NA}$ where n is the refractive index of the scintillating material and NA is the numerical aperture. The resolution of an optical imaging system is limited by diffraction, aberrations and imperfect focus. Denoting the width of the PSF for the optical imaging system to be σ_o, the resolution of the whole system is $\sigma_{\mathrm{tot}} = \sqrt{\sigma_s^2 + \sigma_f^2 + \sigma_o^2}$. In order to obtain a good resolution, a thin detection screen should be selected but doing so will decrease the detection efficiency, so a trade-off between the two considerations is needed. Large numerical aperture will lower the diffraction limit of the optical imaging system but increase σ_f. There is an optimized numerical aperture to minimize σ_{tot}.

Detection efficiency is another key consideration which often competes with spatial resolution. The peak charge flux on the detection screen can be estimated by $F_e \sim Q/(2\pi|M_{x,11}|R_\gamma\gamma\sigma_{x0}\sigma_\gamma)$ where Q is the total charge and σ_γ is the relative rms energy spread. The peak photon flux at the camera is therefore $F_{ph} \sim F_e f_{e\to ph}\mathrm{NA}^2/(2M_o^2)$, where $f_{e\to ph}$ is the conversion efficiency from electrons to photons and M_o is the magnification of the optical imaging system. Here we have assumed that the luminous intensity of the screen satisfies Lambert's cosine law. Therefore the diagnostics should be carefully designed so that F_{ph} is well above the operating threshold of the sensor.

3.6. Energy spread and its correlation with emittance

A broad energy spectrum will also introduce errors into the emittance measurement. The particles with a large energy offset with respect to the central energy do not get well focused. This leads to a very large beam size on the screen and thus the signal-to-noise ratio (SNR) becomes quite poor, which introduces errors when retrieving the emittance using the least squares method. To make this point clear, we performed a simulation using a 200 MeV beam with broad spectrum (20% rms energy spread). As seen in figure 10(a), the bowtie-shaped beam profile has two flanks with very low SNR (the areas denoted by the arrows). The emittance retrieval is carried out using the data within the range of ±20 MeV, ±30 MeV and ±40 MeV around the central energy, respectively. Figure 10(b) shows the fitting results. It can be seen that the fitting result using a narrow energy range matches the simulation result very well, whereas those with a broad energy range significantly deviate from the simulation result. The discussion above indicates that, for broad energy spectrum measurement, data that greatly deviate from the central energy should be avoided, but meanwhile this implies only the emittance of the fraction closed to the central energy can be obtained. Nonetheless, since the method assumes that the geometry emittance is independent of the energy spectrum, the measured value is still a reasonable estimation of the emittance of the whole beam.

However, a beam generated in the PBA more or less has a correlation between the geometry emittance and the energy. The trajectory of a particle in the phase space is dependant on

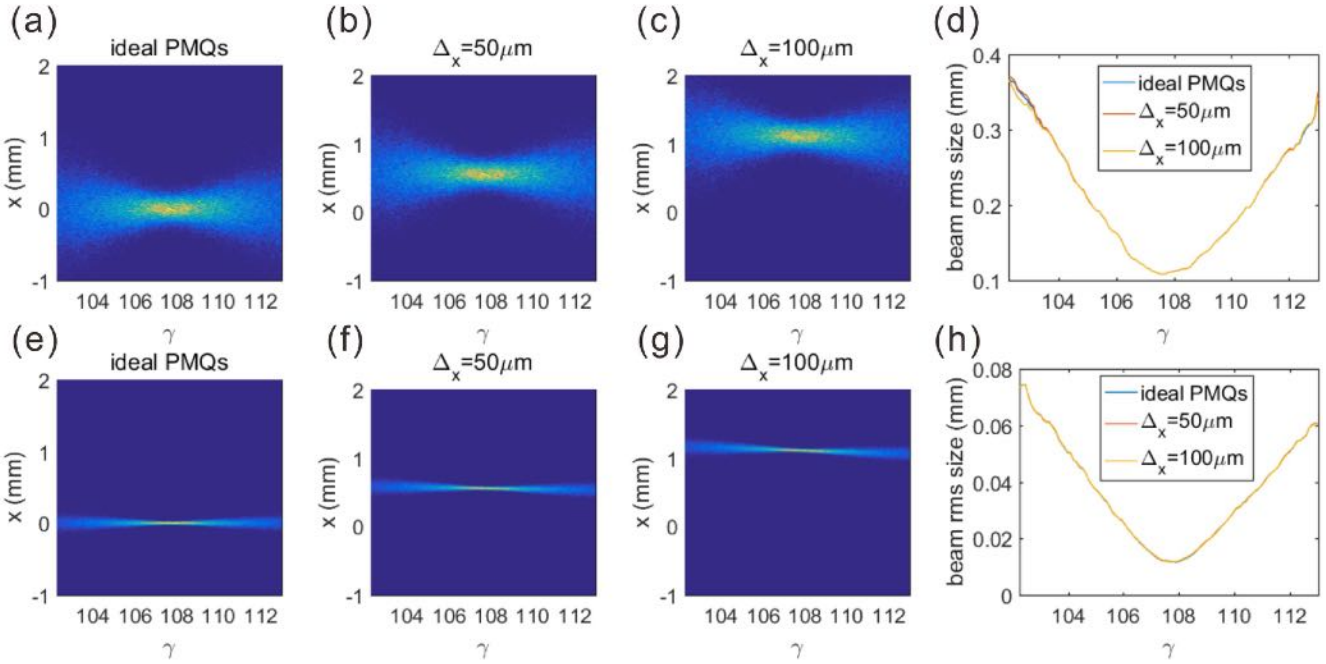

Figure 8. Signals on the detection screen for ideal PMQs and the ones with offset Δ_x. Plots (a)–(d) are for the beams of 2.7 μm rad emittance and plots (e)–(h) are for the beams of 54 nm rad emittance. Beam sizes σ_x as a function of particle energy are plotted in (d) and (h). The other parameters are the same as those in figure 7.

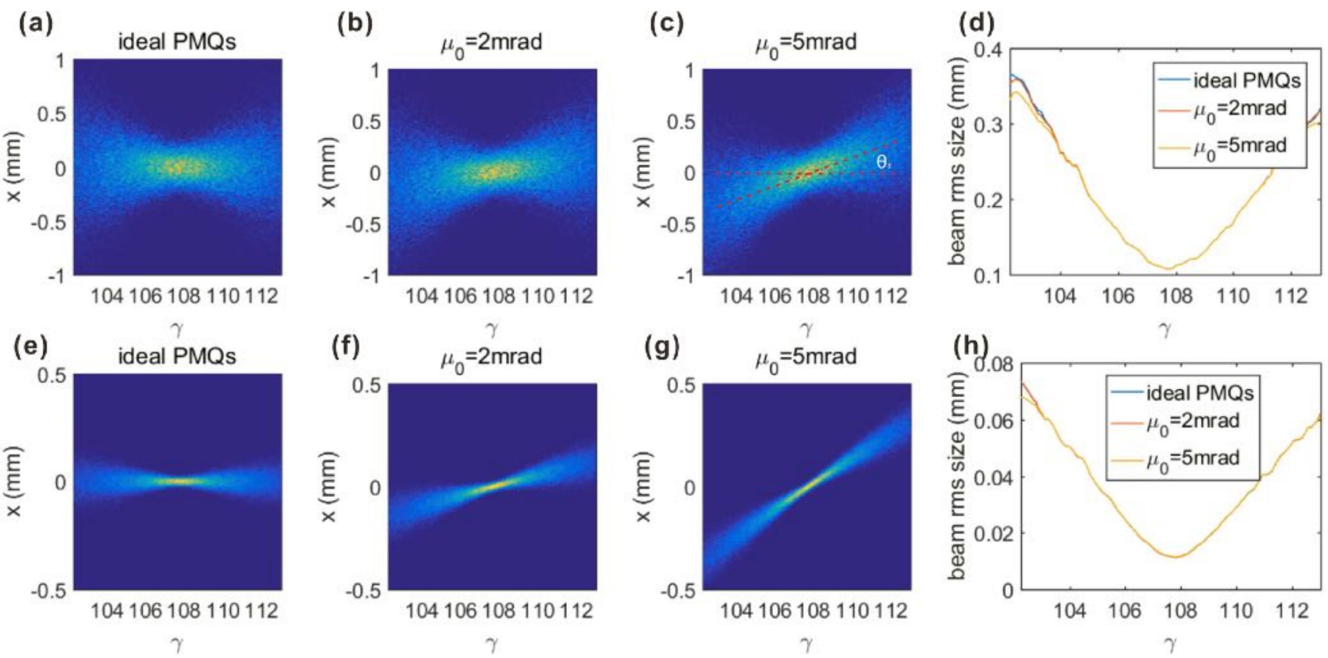

Figure 9. Signals on the detection screen for normal and oblique incident beams. Plots (a)–(d) are for the beams of 2.7 μm rad emittance and plots (e)–(h) are for the beams of 54 nm rad emittance. Beam sizes $\sigma_{\tilde{x}}$ as a function of particle energy are plotted in (d) and (h). The other parameters are the same as those in figure 7.

γ as $x \propto \gamma^{-1/4} \sin \Phi$ and $x' \propto \gamma^{-3/4} \cos \Phi$ where Φ is the betatron phase. This relation can be given by solving the equation of motion during acceleration

$$x'' + \frac{\gamma'}{\gamma} x' + \omega_\beta^2 x = 0, \tag{8}$$

where $\omega_\beta = \omega_p / \sqrt{2\gamma}$ is the betatron frequency and ω_p is the plasma frequency. The γ-dependence implies that the geometry emittance correlates with the energy spectrum. For all that, we point out that this effect can be neglected in the emittance measurement even for a broad energy spectrum. In order to prove it, we initialized two beams in the simulation with one without an ϵ_x-γ correlation while the has one. The two beams have the same projected geometry emittance (0.14 nm rad). The central energy is 200 MeV and the rms energy spread is 10%. Figure 11 shows the simulation results.

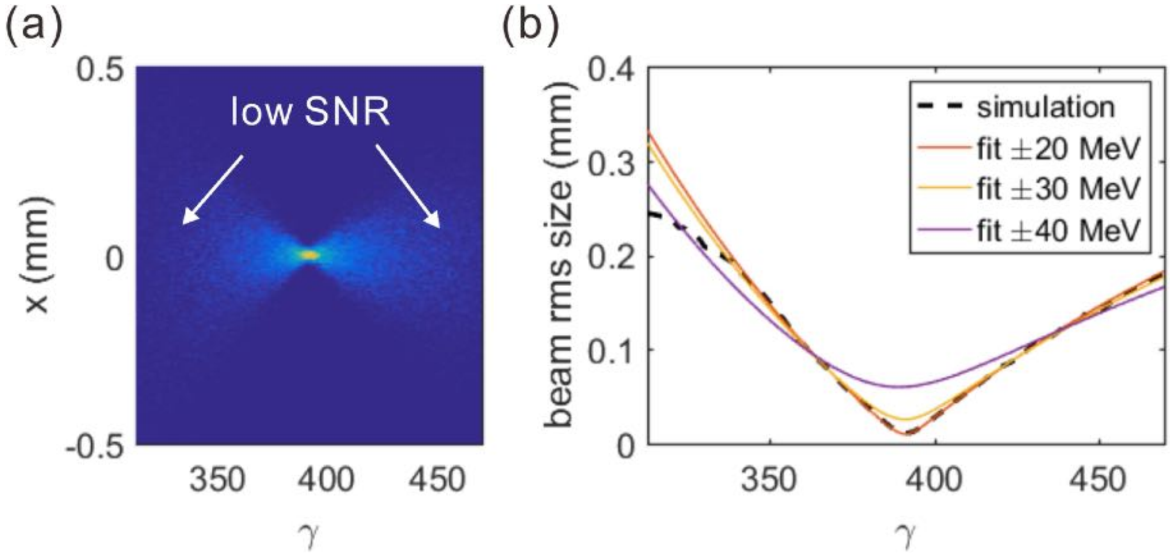

Figure 10. (a) Beam profile for broad energy spectrum with 200 MeV central energy and 20% rms energy spread. (b) Beam size versus energy. The black dashed line represents the simulation results. The solid lines represent the fitting curves using the data within the ranges of ± 20 MeV, ± 30 MeV and ± 40 MeV around the central energy.

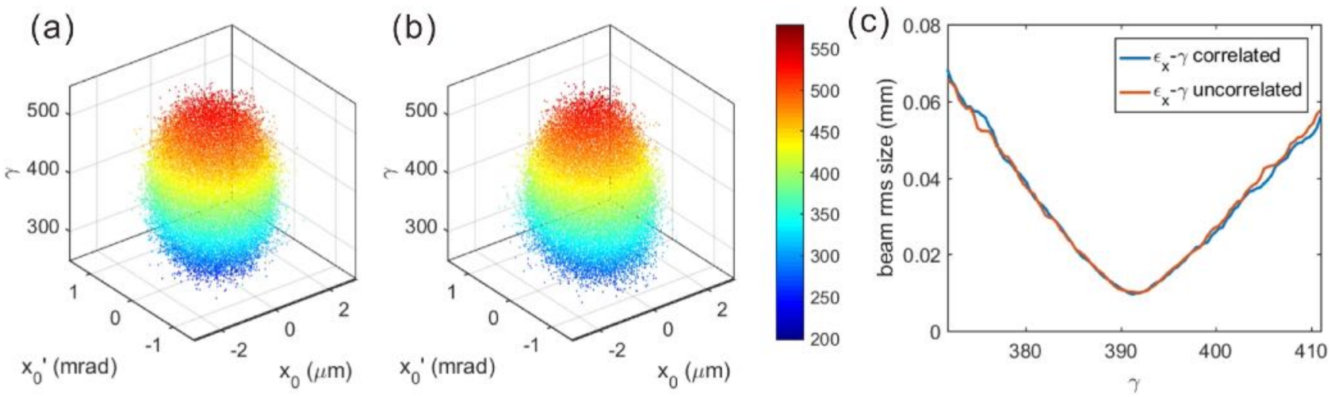

Figure 11. Distributions of (a) ϵ_x-γ uncorrelated beam and (b) correlated beam in x-x'-γ phase space. (c) Beam size versus energy. The blue and red lines correspond to the ϵ_x-γ correlated and uncorrelated beams, respectively.

The simulated beam sizes in figure 11(c) show little difference between the two beams. This indicates that the ϵ_x-γ correlation can be indeed neglected. For a smaller energy spread, this effect becomes more trivial.

4. Conclusion

In this paper, we have systematically discussed the feasibility and reliability of using permanent magnetic quadrupoles for single-shot sub-100 nm rad emittance measurement in plasma-based acceleration. The impact of several nonideal factors in experiments are carefully examined through numerical simulations and theoretical analyses. Angular misalignment of the PMQs is the major source of errors. We derived an error formula for angular misalignment by which one can estimate the error of the measured emittance. For a low emittance measurement of ~100 MeV beams, an angular alignment accuracy of ~0.1° is necessary. This requirement can be eased for higher beam energies. The aberrations caused by the HOFCs are relatively weak for the emittance measurement under current magnet manufacturing and assembly conditions. A series of PMQs has been manufactured and characterized at Tsinghua University. Their HOFCs are tested to be negligible through numerical simulations. Position misalignment of PMQs has been proven to have no contribution to the error of measurement but causes a translational shift of the detected signals. Angular fluctuation of incoming beams also does not affect the measurement precision. The oblique incidence of a beam will cause a rotational shift of the detected signals. By measuring the rotational angle, the incident angle can be deduced. The diagnostics should be properly designed to achieve high spatial resolution and detection efficiency to guarantee the accuracy of sub-100 nm rad emittance measurement. In conclusion, considering the error sources in practice, the PMQ method is capable of measuring sub-100 nm rad emittance.

Acknowledgments

We thank Professor Shuxin Zheng and Mr. Baichuan Wang for beneficial discussions on fabricating and measuring PMQs. This work was supported by NSFC Grant No. 11425521, No. 11535006, No. 11375006, No. 11775125 and No. 11475101, China Academy of Engineering Physics Foundation Grant No. 2014A0102003.

Appendix A. Phase space retrieval based on least squares method

The beam size σ_x on the detection screen is

$$\sigma_x^2 = M_{x,11}^2(\beta_{x0}\epsilon_x) + M_{x,12}^2(\gamma_{x0}\epsilon_x) - 2M_{x,11}M_{x,12}(\alpha_{x0}\epsilon_x). \quad \text{(A.1)}$$

Here the Twiss parameters are defined as $\beta_{x0}\epsilon_x = \langle x_0^2\rangle$, $\gamma_{x0}\epsilon_x = \langle x_0'^2\rangle$ and $\alpha_{x0}\epsilon_x = -\langle x_0 x_0'\rangle$. The beam size σ_x as a function of the particle energy γ is obtained experimentally and the functional relation between $M_{x,ij}$ and γ is also known beforehand. To get a good approximation of the Twiss parameters and the initial emittance, we solve equation (A.1) using the least squares method. The residue function is defined as

$$\eta^2 = \int_{\gamma_0-\delta\gamma}^{\gamma_0+\delta\gamma}(M_{x,11}^2\beta_{x0}\epsilon_x + M_{x,12}^2\gamma_{x0}\epsilon_x - 2M_{x,11}M_{x,12}\alpha_{x0}\epsilon_x - \sigma_x^2)^2 d\gamma, \quad \text{(A.2)}$$

where $(\gamma_0 - \delta\gamma, \gamma_0 + \delta\gamma)$ is the effective energy range measured by the detection screen, and requires

$$\frac{\partial\eta^2}{\partial(\beta_{x0}\epsilon_x)} = 0,\ \frac{\partial\eta^2}{\partial(\gamma_{x0}\epsilon_x)} = 0,\ \frac{\partial\eta^2}{\partial(\alpha_{x0}\epsilon_x)} = 0, \quad \text{(A.3)}$$

which gives

$$\mathbf{S}_x\mathbf{T}_x = \mathbf{\Sigma}_x \quad \text{(A.4)}$$

with $\mathbf{T}_x \equiv \epsilon_x(\beta_{x0}, \gamma_{x0}, \alpha_{x0})^T$,

$$\mathbf{S}_x = \begin{pmatrix} \langle s_1, s_1\rangle & \langle s_1, s_2\rangle & \langle s_1, s_3\rangle \\ \langle s_2, s_1\rangle & \langle s_2, s_2\rangle & \langle s_2, s_3\rangle \\ \langle s_3, s_1\rangle & \langle s_3, s_2\rangle & \langle s_3, s_3\rangle \end{pmatrix} \text{ and } \mathbf{\Sigma}_x = \begin{pmatrix} \langle s_1, \sigma_x^2\rangle \\ \langle s_2, \sigma_x^2\rangle \\ \langle s_3, \sigma_x^2\rangle \end{pmatrix}. \quad \text{(A.5)}$$

Here, for the purpose of simplifying the notations, we define $s_1 = M_{x,11}^2$, $s_2 = M_{x,12}^2$ and $s_3 = -2M_{x,11}M_{x,12}$. The expression $\langle f, g\rangle$ refers to the integral $\int f(\gamma)g(\gamma)d\gamma$. So the Twiss parameters are

$$\mathbf{T}_x = \mathbf{S}_x^{-1}\mathbf{\Sigma}_x \quad \text{(A.6)}$$

and the emittance is

$$\epsilon_x^2 = \mathbf{T}_x^T\mathbf{\Lambda}\mathbf{T}_x = \mathbf{\Sigma}_x^T\mathbf{S}_x^{-1}\mathbf{\Lambda}\mathbf{S}_x^{-1}\mathbf{\Sigma}_x \text{ where } \mathbf{\Lambda} \equiv \begin{pmatrix} 0 & \frac{1}{2} & 0 \\ \frac{1}{2} & 0 & 0 \\ 0 & 0 & -1 \end{pmatrix}. \quad \text{(A.7)}$$

Appendix B. Derivation of measurement error induced by angular misalignment

Firstly, we derive the particle motion in a single quadrupole magnet. When the magnet is rotated by a small angle φ, the motions in both the x and y directions couple together and thus we need to investigate the particle dynamics in the 4D phase space (x, x', y, y'). Assuming the quadrupole magnet provides a focusing force in the x direction and defocusing force in the y direction, the equation of motion for the particle can be written as

$$x'' + B_y/(\rho B) = 0, \quad \text{(B.1)}$$

$$y'' - B_x/(\rho B) = 0, \quad \text{(B.2)}$$

where $\langle\cdot\rangle'$ refers to $\frac{d}{dz}$ and ρB is the magnetic rigidity that is related to the charge–mass ratio and particle energy. According to equations (4) and (5), the quadrupole magnetic fields are

$$B_x = B_{2,\rho}\cos\phi - B_{2,\phi}\sin\phi = B_G\{y\cos(2\varphi) - x\sin(2\varphi)\}, \quad \text{(B.3)}$$

$$B_y = B_{2,\rho}\sin\phi + B_{2,\phi}\cos\phi = B_G\{x\cos(2\varphi) + y\sin(2\varphi)\}, \quad \text{(B.4)}$$

where $B_G \equiv \sqrt{A_2^2 + B_2^2}$ is the field gradient and $\varphi = -\frac{1}{2}\tan^{-1}(B_2/A_2)$. Defining the strength parameter of the magnet as $K \equiv \sqrt{B_G/(\rho B)}$, equations (B.1) and (B.2) are expressed as

$$x'' + K^2\{x\cos(2\varphi) + y\sin(2\varphi)\} = 0, \quad \text{(B.5)}$$

$$y'' - K^2\{y\cos(2\varphi) - x\sin(2\varphi)\} = 0. \quad \text{(B.6)}$$

It can be verified that the solutions can be expressed into a matrix form

$$(x, x', y, y')^T = \mathbf{R}(-\varphi)\mathbf{Q}\mathbf{R}(\varphi)(x_0, x_0', y_0, y_0')^T, \quad \text{(B.7)}$$

where

$$\mathbf{Q} = \begin{pmatrix} \mathbf{Q}_x & \mathbf{0} \\ \mathbf{0} & \mathbf{Q}_y \end{pmatrix} \quad \text{(B.8)}$$

is the 4D transport matrix for an aligned quadrupole magnet with

$$\mathbf{Q}_x = \begin{pmatrix} \cos(Kl) & \frac{1}{K}\sin(Kl) \\ -K\sin(Kl) & \cos(Kl) \end{pmatrix}, \quad \text{(B.9)}$$

$$\mathbf{Q}_y = \begin{pmatrix} \cosh(Kl) & \frac{1}{K}\sinh(Kl) \\ K\sinh(Kl) & \cosh(Kl) \end{pmatrix}, \quad \text{(B.10)}$$

and l is the length. For the quadrupole magnets that focus in the y direction and defocus in the x direction, a similar form of the transport matrix is obtained only by replacing K with iK where $i^2 = -1$. The rotation matrix $\mathbf{R}(\varphi)$ is defined as

$$\mathbf{R}(\varphi) = \begin{pmatrix} \cos\varphi & 0 & \sin\varphi & 0 \\ 0 & \cos\varphi & 0 & \sin\varphi \\ -\sin\varphi & 0 & \cos\varphi & 0 \\ 0 & -\sin\varphi & 0 & \cos\varphi \end{pmatrix}. \tag{B.11}$$

According to equation (B.7), passing through an angularly misaligned quadrupole magnet can be also interpreted as rotating the phase space by φ before entering and rotating it back by $-\varphi$ right after the exitance, which coincides with our intuitive understanding. Since $\varphi \ll 1$, using $\cos\varphi \simeq 1$ and $\sin\varphi \simeq \varphi$, $\mathbf{R}(\varphi)$ can be expanded as $\mathbf{R}(\varphi) \simeq \mathbf{I} + \varphi\mathbf{J}$, where

$$\mathbf{J} \equiv \begin{pmatrix} \mathbf{0} & \mathbf{I}_{2\times 2} \\ -\mathbf{I}_{2\times 2} & \mathbf{0} \end{pmatrix}. \tag{B.12}$$

The transport matrix of the misaligned magnet is therefore

$$\begin{aligned} \tilde{\mathbf{Q}} = \mathbf{R}(-\varphi)\mathbf{Q}\mathbf{R}(\varphi) &\simeq \mathbf{Q} \\ &+ \varphi(\mathbf{QJ} - \mathbf{JQ}) = \mathbf{Q} + \varphi\Delta\mathbf{Q}. \end{aligned} \tag{B.13}$$

where

$$\Delta\mathbf{Q} = \begin{pmatrix} \mathbf{0} & \mathbf{Q}_x - \mathbf{Q}_y \\ \mathbf{Q}_y - \mathbf{Q}_x & \mathbf{0} \end{pmatrix}. \tag{B.14}$$

Now we calculate the transport matrix of the beamline and then estimate the measurement error. Consider a beamline consisting of N PMQs and its transport matrix with each PMQ rotated by φ_i is

$$\begin{aligned} \tilde{\mathbf{M}} &= \mathbf{D}_{N+1}\tilde{\mathbf{Q}}_N\mathbf{D}_N \cdots \tilde{\mathbf{Q}}_1\mathbf{D}_1 \\ &\simeq \mathbf{M} + \sum_i \varphi_i \mathbf{D}_{N+1}\mathbf{Q}_N\mathbf{D}_N \cdots \Delta\mathbf{Q}_i \cdots \mathbf{Q}_1\mathbf{D}_1 \\ &= \mathbf{M} + \sum_i \varphi_i \Delta\mathbf{M}_i. \end{aligned} \tag{B.15}$$

Here $\mathbf{M}$ is the matrix of the aligned beamline and $\mathbf{D}_i$ is the transport matrix for the drifting sections, which are written as

$$\mathbf{M} = \begin{pmatrix} \mathbf{M}_x & \mathbf{0} \\ \mathbf{0} & \mathbf{M}_y \end{pmatrix} \tag{B.16}$$

and

$$\mathbf{D}_i = \begin{pmatrix} \mathbf{D}^{(i)} & \mathbf{0} \\ \mathbf{0} & \mathbf{D}^{(i)} \end{pmatrix} \text{ with } \mathbf{D}^{(i)} = \begin{pmatrix} 1 & L_i \\ 0 & 1 \end{pmatrix}. \tag{B.17}$$

Note that $\mathbf{D}_i$ and $\mathbf{Q}_i$ are block diagonal matrices and $\Delta\mathbf{Q}_i$ is a block skew-diagonal matrix, $\Delta\mathbf{M}_i$ is therefore a block skew-diagonal matrix expressed as

$$\Delta\mathbf{M}_i = \begin{pmatrix} \mathbf{0} & \Delta\mathbf{M}_{xy}^{(i)} \\ \Delta\mathbf{M}_{yx}^{(i)} & \mathbf{0} \end{pmatrix} \tag{B.18}$$

with

$$\begin{aligned} \Delta\mathbf{M}_{xy}^{(i)} = &(\mathbf{D}^{(N+1)}\mathbf{Q}_x^{(N)}\mathbf{D}^{(N)} \cdots \mathbf{Q}_x^{(i+1)}\mathbf{D}^{(i+1)})(\mathbf{Q}_x^{(i)} - \mathbf{Q}_y^{(i)}) \\ &\times (\mathbf{D}^{(i)}\mathbf{Q}_y^{(i-1)}\mathbf{D}^{(i-1)} \cdots \mathbf{Q}_y^{(1)}\mathbf{D}^{(1)}). \end{aligned} \tag{B.19}$$

Exchanging the subscripts 'x' and 'y' gives $\Delta\mathbf{M}_{yx}^{(i)}$. Combining equations (B.15), (B.16) and (B.18), we have

$$\tilde{\mathbf{M}} = \begin{pmatrix} \mathbf{M}_x & \sum_i \varphi_i \Delta\mathbf{M}_{xy}^{(i)} \\ \sum_i \varphi_i \Delta\mathbf{M}_{yx}^{(i)} & \mathbf{M}_y \end{pmatrix}. \tag{B.20}$$

Having known the transport matrix dependence on φ_i and following the notations in appendix A, we found

$$\begin{aligned} \sigma_x^2 = &\epsilon_x(s_{x,1}\beta_{x0} + s_{x,2}\gamma_{x0} + s_{x,3}\varphi_{x0}) \\ &+ \epsilon_y \sum_i \varphi_i^2 (\Delta s_{xy,1}^{(i)}\beta_{y0} \\ &+ \Delta s_{xy,2}^{(i)}\gamma_{y0} + \Delta s_{xy,3}^{(i)}\varphi_{y0}), \end{aligned} \tag{B.21}$$

where $\Delta s_{xy,1}^{(i)} = (\Delta M_{xy,11}^{(i)})^2$, $\Delta s_{xy,2}^{(i)} = (\Delta M_{xy,12}^{(i)})^2$ and $\Delta s_{xy,3}^{(i)} = -2\Delta M_{xy,11}^{(i)}\Delta M_{xy,12}^{(i)}$. This expression is derived based on the assumption that the initial transverse phase spaces are decoupled. Following similar steps for the derivation of the least squares solutions in appendix A and skipping the tedious mathematics therein, we have

$$\mathbf{S}_x\mathbf{T}_x + \sum_i \varphi_i^2 \Delta\mathbf{S}_{xy}^{(i)}\mathbf{T}_y = \mathbf{\Sigma}_x, \tag{B.22}$$

where $\mathbf{T}_y = \epsilon_y(\beta_{y0}, \gamma_{y0}, \varphi_{y0})^T$ and the elements of $\Delta\mathbf{S}_{xy}^{(k)}$ is $\Delta S_{xy,ij}^{(k)} = \langle s_{x,i}, \Delta s_{xy,j}^{(k)} \rangle$. Since the real Twiss parameters $\mathbf{T}_y$ are unknown in a single measurement, one needs some *a priori* assumptions for $\mathbf{T}_y$ or utilizes the measured $\tilde{\mathbf{T}}_y$ by solving $\mathbf{S}_y\tilde{\mathbf{T}}_y = \mathbf{\Sigma}_y$ in a separate experiment. $\tilde{\mathbf{T}}_y$ usually has no significant difference from $\mathbf{T}_y$, so it is reasonable to use $\tilde{\mathbf{T}}_y$ as a substitute. According to equation (B.22), the measured Twiss parameters are

$$\tilde{\mathbf{T}}_x = \mathbf{T}_x + \mathbf{S}_x^{-1}\sum_i \varphi_i^2 \Delta\mathbf{S}_{xy}^{(i)}\tilde{\mathbf{T}}_y, \tag{B.23}$$

and its partial derivative with respect to φ_i^2 is

$$\frac{\partial\tilde{\mathbf{T}}_x}{\partial\varphi_i^2} = \mathbf{S}_x^{-1}\Delta\mathbf{S}_{xy}^{(i)}\tilde{\mathbf{T}}_y. \tag{B.24}$$

Using the relationship $\tilde{\epsilon}_x^2 = \tilde{\mathbf{T}}_x^T\mathbf{\Lambda}\tilde{\mathbf{T}}_x$, we can get the system error induced by the angular alignment errors $\sigma_{\varphi_i^2}$

$$\sigma_{\epsilon_x}^2 = \frac{1}{4}\frac{\sum_i ((\mathbf{S}_x^{-1}\Delta\mathbf{S}_{xy}^{(i)}\tilde{\mathbf{T}}_y)^T\mathbf{\Lambda}\tilde{\mathbf{T}}_x + \tilde{\mathbf{T}}_x^T\mathbf{\Lambda}\mathbf{S}_x^{-1}\Delta\mathbf{S}_{xy}^{(i)}\tilde{\mathbf{T}}_y)^2\sigma_{\varphi_i^2}^2}{\tilde{\mathbf{T}}_x^T\mathbf{\Lambda}\tilde{\mathbf{T}}_x}. \tag{B.25}$$

Appendix C. Proof of independence between measurement error and position misalignments of PMQs

This appendix derives the emittance error induced by the position errors of PMQs. Assuming the transverse offset of a PMQ is Δ_x, the particle motion is

$$x'' + K^2 x = K^2\Delta_x. \tag{C.1}$$

The matrix form of the solution is

$$(x, x', 1)^T = \tilde{\mathbf{Q}}_x(x_0, x_0', 1)^T \text{ with } \tilde{\mathbf{Q}}_x = \begin{pmatrix} \mathbf{Q}_x & \mathbf{\Delta}_x \\ \mathbf{0} & 1 \end{pmatrix}, \tag{C.2}$$

where $\mathbf{\Delta}_x = (\Delta_x, 0)^T$ and $\mathbf{Q}_x$ is the transport matrix for an ideal quadrupole which is defined in appendix B. Letting $\Delta_{x,i}$ be the offset of ith quadrupole magnet and defining the transport matrices of the quadrupoles and drifting sections as

$$\tilde{\mathbf{Q}}_x^{(i)} = \begin{pmatrix} \mathbf{Q}_x^{(i)} & \mathbf{\Delta}_x^{(i)} \\ \mathbf{0} & 1 \end{pmatrix} \quad \text{and} \quad \mathbf{D}^{(i)} = \begin{pmatrix} \mathbf{D}_i & \mathbf{0} \\ \mathbf{0} & 1 \end{pmatrix}, \tag{C.3}$$

we can write the transport matrix of the system as

$$\tilde{\mathbf{M}}_x = \mathbf{D}^{(N+1)}\tilde{\mathbf{Q}}_x^{(N)}\mathbf{D}^{(N)} \cdots \tilde{\mathbf{Q}}_x^{(1)}\mathbf{D}^{(1)} \simeq \begin{pmatrix} \mathbf{M}_x & \sum_i \mathbf{m}_x^{(i)}\mathbf{\Delta}_x^{(i)} \\ \mathbf{0} & 1 \end{pmatrix}, \tag{C.4}$$

where

$$\mathbf{m}_x^{(i)} = \prod_{j=i+1}^{N} \mathbf{D}_{j+1}\mathbf{Q}_x^{(j)},\ (i < N) \quad \text{and} \quad \mathbf{m}_x^{(N)} = \mathbf{I}. \tag{C.5}$$

Having known the transport matrix of the system, the beam's position on the detection screen is found to be

$$x = M_{x,11}x_0 + M_{x,12}x_0' + \sum_i m_{x,11}^{(i)}\Delta_{x,i}. \tag{C.6}$$

Although the new position $\tilde{x}$ is shifted by $\sum_i m_{x,11}^{(i)}\Delta_{x,i}$, the beam size does not vary because the relation $\tilde{x} = M_{x,11}x_0 + M_{x,12}x_0'$ yields

$$\sigma_{\tilde{x}}^2 = \epsilon_x(s_{x,1}\beta_{x0} + s_{x,2}\gamma_{x0} + s_{x,3}\alpha_{x0}). \tag{C.7}$$

Therefore the measurement of beam emittance will not be affected by the position alignment of the PMQs.

References

[1] Weingartner R *et al* 2012 *Phys. Rev. Spec. Top. Accel. Beams* **15** 111302
[2] Tajima T and Dawson J M 1979 *Phys. Rev. Lett.* **43** 267
[3] Chen P, Dawson J M, Huff R W and Katsouleas T 1985 *Phys. Rev. Lett.* **54** 693–6
[4] Leemans W P, Nagler B, Gonsalves A J, Toth C, Nakamura K, Geddes C G R, Esarey E, Schroeder C B and Hooker S M 2006 *Nat. Phys.* **2** 696–9
[5] Blumenfeld I *et al* 2007 *Nature* **445** 741–4
[6] Leemans W P *et al* 2014 *Phys. Rev. Lett.* **113** 245002
[7] Litos M *et al* 2014 *Nature* **515** 92–5
[8] Rosenzweig J B, Breizman B, Katsouleas T and Su J J 1991 *Phys. Rev.* A **44** R6189–92
[9] Lu W, Huang C, Zhou M, Mori W B and Katsouleas T 2006 *Phys. Rev. Lett.* **96** 165002
[10] Kneip S *et al* 2010 *Nat. Phys.* **6** 980–3
[11] Brunetti E *et al* 2010 *Phys. Rev. Lett.* **105** 215007
[12] Plateau G R *et al* 2012 *Phys. Rev. Lett.* **109** 064802
[13] Kneip S *et al* 2012 *Phys. Rev. Spec. Top. Accel. Beams* **15** 021302
[14] Hidding B, Pretzler G, Rosenzweig J B, Knigstein T, Schiller D and Bruhwiler D L 2012 *Phys. Rev. Lett.* **108** 035001
[15] Li F *et al* 2013 *Phys. Rev. Lett.* **111** 015003
[16] Xu X L *et al* 2014 *Phys. Rev. Spec. Top. Accel. Beams* **17** 061301
[17] Xu X, Li F, An W, Yu P, Lu W, Joshi C and Mori W 2016 arXiv:1610.00788
[18] Antici P 2012 *J. Appl. Phys.* **112** 044902
[19] Xu X L *et al* 2016 *Phys. Rev. Lett.* **116** 124801
[20] Fritzler S, Lefebvre E, Malka V, Burgy F, Dangor A E, Krushelnick K, Mangles S P D, Najmudin Z, Rousseau J P and Walton B 2004 *Phys. Rev. Lett.* **92** 165006
[21] Sears C M S, Buck A, Schmid K, Mikhailova J, Krausz F and Veisz L 2010 *Phys. Rev. Spec. Top. Accel. Beams* **13** 092803
[22] Schnell M *et al* 2012 *Phys. Rev. Lett.* **108** 075001
[23] Golovin G, Banerjee S, Liu C, Chen S, Zhang J, Zhao B, Zhang P, Veale M, Wilson M and Seller P 2016 *Sci. Rep.* **6** 24622
[24] Manahan G G *et al* 2014 *New J. Phys.* **16** 103006
[25] Cianchi A *et al* 2013 *Nucl. Instrum. Methods Phys. Res., Sect. A* **720** 153–6
[26] Lee S Y 2004 *Accelerator Physics* 2nd edn (Singapore: World Scientific)
[27] Eichner T, Grner F, Becker S, Fuchs M, Habs D, Weingartner R, Schramm U, Backe H, Kunz P and Lauth W 2007 *Phys. Rev. Spec. Top. Accel. Beams* **10** 082401
[28] Lim J K, Frigola P, Travish G, Rosenzweig J B, Anderson S G, Brown W J, Jacob J S, Robbins C L and Tremaine A M 2005 *Phys. Rev. Spec. Top. Accel. Beams* **8** 072401
[29] Halbach K 1980 *Nucl. Instrum. Meth.* **169** 1–10
[30] Becker S *et al* 2009 *Phys. Rev. Spec. Top. Accel. Beams* **12** 102801
[31] Arpaia P, Buzio M, Perez J G, Petrone C, Russenschuck S and Walckiers L 2012 *J. Instrum.* **7** P05003
[32] Eidelman S *et al* 2004 *Phys. Lett.* B **592** 1–5
[33] Murokh A, Rosenzweig J, Yakimenko V, Johnson E and Wang X J 1999 Limitations on the resolution of YAG:Ce beam profile monitor for high brightness electron beam *The Physics of High Brightness Beams. Proceedings, 2nd ICFA Advanced Accelerator Workshop (Los Angeles, USA, November 9–12, 1999)* 564–80